Letter

Reduction of the electron-beam divergence of laser wakefield accelerators by integrated plasma lenses

Y.-Y. Chang,[1,*] J. Couperus Cabadağ,[1] A. Debus,[1] A. Ghaith,[1] M. LaBerge,[1,2] R. Pausch,[1] S. Schöbel,[1,3] P. Ufer,[1,3] U. Schramm,[1,3] and A. Irman[1]

[1] *Helmholtz-Zentrum Dresden-Rossendorf, Bautzner Landstraße 400, 01328 Dresden, Germany*
[2] *Physics Department, University of Texas-Austin, Austin, Texas 78712, USA*
[3] *Technische Universität Dresden, 01062 Dresden, Germany*

(Received 25 August 2023; accepted 1 November 2023; published 4 December 2023)

We report on electron-beam collimation using a passive plasma lens, integrated directly and conveniently into a laser wakefield-accelerator stage operating in the high-charge regime. The lens is created by the reshaping of the gas-density profile of a supersonic jet at the beam's exit side through an obstacle mounted above the jet. It reduces the beam's divergence by a factor of 2 to below 1 mrad (rms), while preserving the total charge of 170 pC and maintaining the energy spread. The resulting spectral-charge density, defined here as the charge per energy bandwidth and emission angle, of up to 7 pC/MeV mrad played a key role in the recent experimental demonstration of free-electron lasing. The simple and robust gas-shaping technique presented holds the potential to generate specific density profiles, which are essential for the application of adiabatic focusing or staging of accelerators.

DOI: 10.1103/PhysRevApplied.20.L061001

Introduction. Laser-driven plasma accelerators (LPAs) are capable of supporting accelerating fields on the order of 100 GV/m [1], which can be used to accelerate electrons to a few gigaelectronvolts [2] within several centimeters. This technology represents a promising approach for compact accelerators to support applications such as free-electron lasers (FELs) [3,4] and electron-positron colliders [5]. State-of-the-art LPA beams have special properties, such as short duration (20 fs or less) [6–8], high peak current (greater than kiloamperes) [9,10], and small normalized emittance (less than 1 mm mrad) [11,12], yet the relatively large beam divergence (typically around 2 mrad) for a micron-scale source diameter and energy spread (from 10% to 20%) make it difficult to transport such beams through conventional magnetic lattices [13]. The transverse beam size, for example, can increase by about 60-fold after 1-cm drift in a vacuum [14], which, combined with energy spread, drastically degrades beam quality, such as normalized emittance, over a short distance [15]. Although it has been demonstrated that LPA beams can be transported to downstream applications such as synchrotron sources [16–19] or even FELs [3,4], it is essential to develop methods to confine the divergence or energy spread (or both) and minimize the emittance growth of the beam in the immediate proximity of the exit of LPAs.

The idea of using plasmas to focus relativistic electron beams was proposed decades ago [20,21], and plasma lenses have been implemented in conventional accelerators [22–26] and plasma-based accelerators [27–30]. When an electron beam enters a plasma, the azimuthally symmetric transverse field induced either by the plasma shielding around the beam (in overdense plasma) [29] or by the ion cavity created by a driver [27,31] or the beam itself (in underdense plasma) [30] effectively focuses the beam (so-called passive plasma lens). Field gradients reach millions of teslas per meter as opposed to hundreds of teslas per meter in conventional quadrupoles [21]. Electron beams were also sent to a preformed plasma channel induced by externally controlled currents [28,32,33], which provides more tunability of the focusing parameters (so-called active plasma lens). In previous studies of LPAs, improvement of electron-beam parameters was demonstrated by control of the injection and acceleration with use of density-tailored plasma [34–37]. Here we tailor the plasma density behind an LPA stage to generate a shallow density bump, which serves as a plasma lens that collimates the output electron beams. This passive-plasma-lens effect preserves the total beam charge, resulting in energetic electron beams with higher peak spectral-charge densities. This paves the way for independent beam manipulation, minimizing the coupling between the acceleration process and beam extraction.

Experimental setup. The experiment was performed with the 100-TW DRACO (Dresden Laser Acceleration Source) laser system at Helmholtz-Zentrum Dresden-Rossendorf. The laser pulse energy is 2.3 J on

*y.chang@hzdr.de

TABLE I. Electron-beam parameters after optimization of the plasma lens. Each set is collected from ten consecutive shots.

Setting	Peak charge density (pC/MeV mrad)	Horizontal divergence (mrad)	Peak energy (MeV) [energy spread (%)]	Charge within FWHM (pC)
2.5-mm jet, no plasma lens	1.8 ± 0.7	2.1 ± 0.4	203 ± 19 [15]	171 ± 61
2.5-mm jet, with plasma lens ($\phi = 30°$)	4.7 ± 0.8	1.0 ± 0.2	195 ± 8 [13]	185 ± 31
2-mm jet, no plasma lens	1.2 ± 0.6	2 ± 0.2	163 ± 24 [21]	137 ± 27
2-mm jet, with plasma lens ($\phi = 0°$)	1.1 ± 0.3	1.1 ± 0.2	169 ± 45 [31]	93 ± 38
2-mm jet, with plasma lens ($\phi = 15°$)	2.1 ± 0.3	0.8 ± 0.2	158 ± 22 [30]	118 ± 20
2-mm jet, with plasma lens ($\phi = 30°$)	2.7 ± 0.6	1.2 ± 0.2	159 ± 18 [18]	128 ± 21

the target with a pulse duration of 30 fs [full width at half maximum (FWHM)]. The focal spot size is 21 μm (FWHM) with use of an off-axis parabolic mirror (f /20), which provides a normalized peak intensity a_0 of approximately 2.6. The laser pulse is focused above a supersonic de Laval nozzle, composed of helium gas doped with 1% nitrogen, and the backing pressure is set to 11 bar, leading to a plateau plasma density of 2.3×10^{18} cm^{-3}. To measure the energy distribution of the generated electron beams, an electron-energy spectrometer is used, which was designed for point-to-point imaging using the focusing effect of a permanent magnetic dipole [41]. The energy dispersion plane of the spectrometer is perpendicular to the drive-laser polarization. Absolute-charge-calibrated LANEX screens [42] are accordingly positioned to obtain the optimum energy resolution. The nominal accelerated electron beam is optimized with use of self-truncated ionization injection [43], where a quasimonoenergetic bunch is achieved by optimization of the beam-loading effect [10,44]. To match the beam parameters for the

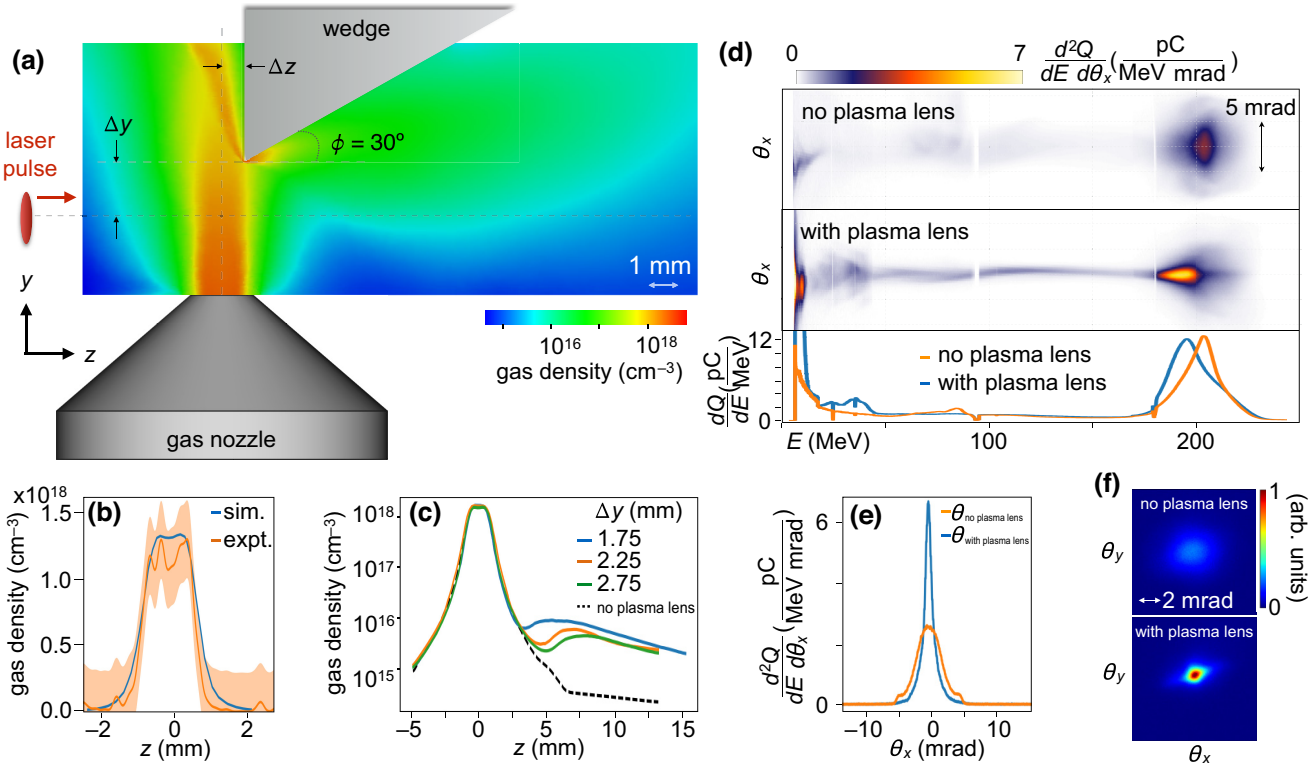

FIG. 1. Simulation (sim.) results obtained with ANSYS FLUENT [38] and experimental electron-beam data. (a) Experimental setup and the gas-density distribution. The drive laser is linearly polarized along the x-axis and travels from left to right. The width of the nozzle is 2.5 mm and the wedge position is adjusted to optimize the electron-beam parameters ($\Delta y = 1.75$, $\Delta z = 0.75$ mm). (b) Comparison of gas density along the laser axis between simulation and experimental measurement when there is no wedge. The experimental measurement is extracted with use of interferometry techniques [39]. The colored region shows the standard error of the measurement over 20 recorded data. (c) Simulated gas-density profile along the laser axis with different Δy when $\Delta z = 0.75$ mm. (d) Electron spectra of representative shots. The top spectrum refers to no plasma lens and the middle spectrum refers to the wedge being at the optimal position. The bottom plot shows the charge distribution integrated over ±17 mrad of the two shots. (e) Divergence at the peak energy of shots in (d). (f) Electron-beam profiles with and without the plasma lens. For these representative shots, the beam divergence is reduced from 1.7 mrad rms (1.4 mrad rms) to 0.6 mrad rms (0.5 mrad rms) in the x plane (y plane). Note that elongation of the beam profile along the laser polarization axis (x axis) is typical for the ionization-injection scheme (see Ref. [40]).

COXINEL (coherent x-ray source inferred from electrons accelerated by laser) beamline [18,19], which is a conventional electron-beam transport line for electron-beam phase-space manipulation aiming for free-electron lasing in the ultraviolet range, a nozzle of width 2.5 mm is used. After optimization, the mean peak energy of the beam is 203 MeV with a statistical standard deviation of 19 MeV, and the mean charge within the FWHM of the energy distribution around the peak is 171 ± 61 pC. The mean divergence and peak charge density are 2.1 ± 0.4 mrad (rms) and 1.8 ± 0.7 pC/MeV mrad, respectively (Table I). A small metal wedge, covering an area of 1 cm^2, is placed a few millimeters above the nozzle [see Fig. 1(a)]. This wedge guides the gas flow and generates a bump behind the LPA region with reduced gas density, serving as a plasma lens for the electron beams that emerge. Empirically, metal wedges with three different angles ϕ (0°, 15°, and 30°) with respect to the laser propagation axis are implemented. The electron-beam spectral-charge density is optimized by our scanning of the position of the wedges, i.e., height and longitudinal position along the beam. After optimization of each wedge, the highest spectral-charge density is obtained for a wedge angle ϕ of 30°. A comparison with different wedge angles can be found in the section 'Comparison with different wedge angles."

To understand the formation of the gas-density profile, we perform hydrodynamic simulations using ANSYS FLUENT [38,45] (see Supplemental Material [46]). The fidelity of the simulations is confirmed by our comparing the results with an independent interferometry measurement where there is no wedge [see Fig. 1(b)]. Afterwards, the wedge is introduced into the simulation. When the supersonic gas flows out of the nozzle and encounters the edge of the wedge, most of the gas continues to stream upward. For example, for a wedge angle ϕ of 30°, a fraction of the gas is guided by the surface of the wedge and creates the shallow density bump along the laser axis behind the LPA. The amplitude of the shallow density bump ranges from 2×10^{15} to 8×10^{15} cm^{-3} and the peak location varies from 3 to 6 mm from the edge of the nozzle [see Fig. 1(c)] depending on the relative location of the wedge.

Experimental results and discussion. Figures 2 demonstrates how the electron-beam divergence and spectral-charge density can be influenced by adjustment of the horizontal and vertical positions of the 30° wedge. Both the magnitude and the location of the density bump are affected, as shown in Fig. 1(c). The smallest beam divergence and thus the highest charge density are achieved when $\Delta y = 1.75$ mm and $\Delta z = 0.75$ mm, i.e., the mean horizontal beam divergence and peak charge density are 1.0 ± 0.2 mrad and 4.7 ± 0.8 pC/MeV mrad, respectively. In this case, the mean peak energy is 195 ± 8 MeV, which is generally a few percent lower than the

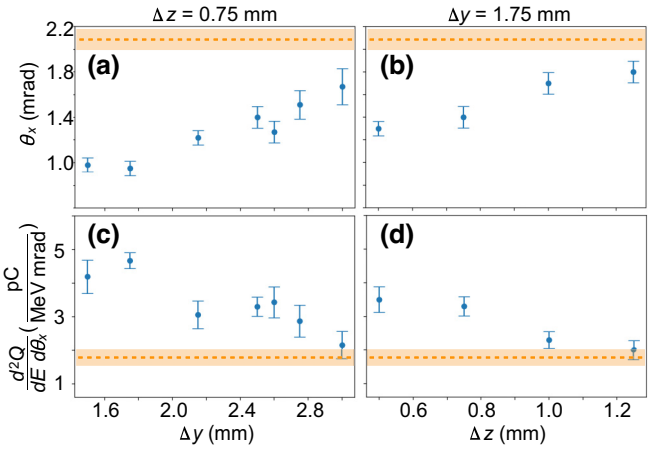

FIG. 2. Electron-beam optimization with the 30°-wedge-position scan. The error bars represent the standard error of the mean and the dashed orange line (area) shows the mean value (standard error) when there is no wedge. (a),(b) Divergence. (c),(d) Peak charge density. Each data point is taken from ten consecutive shots.

original value (see Table I), but beam charge and energy spread are preserved. In addition to the electron spectrometer measurements, Fig. 1(f) exemplifies significantly different beam sizes, measured by a LANEX screen 1.2 m downstream, with and without the plasma lens. The process of the focusing effect is further investigated with use of 3D particle-in-cell simulations (PIConGPU code [47–49]). The results are shown in Fig. 3. The simulation closely approximates the experimental parameters when the 30° wedge is used at the optimized position. It can be seen that the residual laser intensity is still sufficiently high ($a_0 \sim 2$) to ionize the gas and to drive a linear wakefield when the laser enters the density bump [Fig. 3(c)]. Meanwhile, the electron bunch is intense enough to excite its own plasma wave, which indicates a mixed regime of a laser-driven and a beam-driven wakefield. However, the laser intensity dies out quickly as the laser beam diverges immediately behind the initial accelerator. At the same time, the electron bunch dominates the wakefield generation [see Fig. 3(d)] in the low-density region, which creates a field that focuses the bunch. Consequently, the focusing force experienced by the bunch transits smoothly from the laser-driven regime to the beam-driven regime, which ultimately collimates the bunch and decreases the divergence.

The focusing-force transition from the laser-driven regime to the beam-driven regime can be explained with theoretical models. For the laser-driven regime, the equation of transverse motion of an electron in the linear wake can be expressed as [50]

$$x'' = -\frac{k_{\mathrm{foc}}^2 Z_R^2}{z^2} x, \tag{1}$$

where Z_R is the Rayleigh length and $k_{\mathrm{foc}}^2 = \eta a_0(z_0)^2 \sin(k_p d)/\gamma_b w(z_0)^2$, where γ_b is the Lorentz factor of the electron beams, $a_0(z_0)$ and $w(z_0)$ are the normalized peak field strength and the spot size of the drive laser at the exit of the nozzle, respectively, d is the distance from the drive laser to the electron beam, and $\eta = \sqrt{2\pi}(k_p\sigma_z)e^{-k_p^2\sigma_z^2/2}$, where k_p is the plasma wave number and σ_z is the rms length of the drive laser. For the beam-driven regime (passive plasma lens), the equation of transverse motion of an electron in a bubble can be expressed as [30,51]

$$x'' = -k_\beta^2 x, \tag{2}$$

where $k_\beta = k_p/\sqrt{2\gamma_b}$. The theoretical models show that the focusing force from the laser-driven wake scales with the laser intensity, which dominates for a short period but decreases rapidly when the laser intensity dies out. On the other hand, the focusing force from the beam-driven regime scales with plasma density. Therefore, the focusing force is preserved for millimeters with the presence of the density bump.

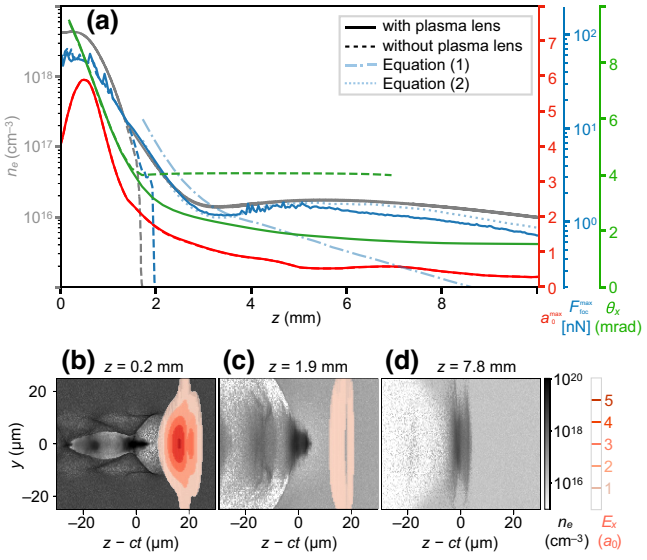

FIG. 3. Results of the particle-in-cell simulation with the PIConGPU code [47]. (a) Evolution of the laser and electron-beam parameters along the propagation axis (z) with (solid line) and without (dashed line) a plasma lens. The jet center is located at $z = 0$. The normalized peak field strength of the laser is shown in red, while the extracted focusing force is plotted in blue. The force is compared with the theoretical predictions, Eqs. (1) and (2). The changes in beam divergence are shown in green. (b)–(d) Plasma density and laser field strength for the case with a plasma lens. The snapshots illustrate the transition from (b) the laser-driven regime to (c) the mixed regime and to (d) the beam-dominated regime. The details of the simulation setup can be found in Refs. [47–49]. For Eqs. (1) and (2), $a_0(z_0) = 2$, $w_0(z_0) = 15$ μm, $\sigma_z = 5$ μm, $Z_R = 2.2$ mm, $d = 5$ μm, and $\gamma_b = 400$.

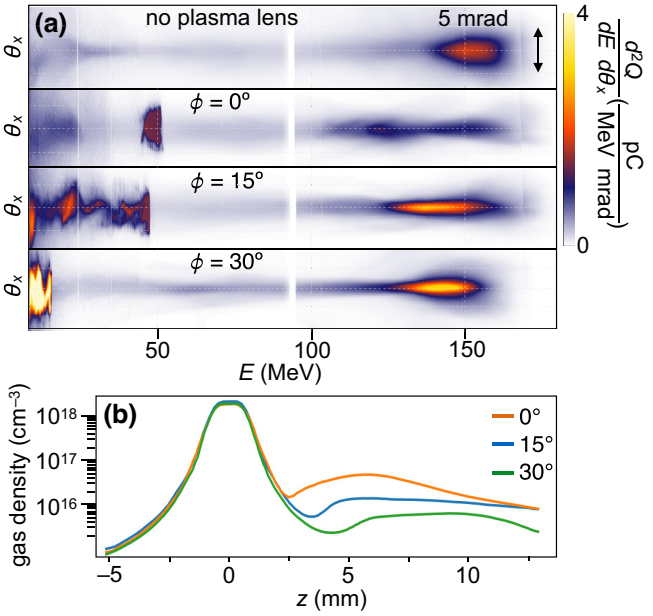

FIG. 4. Electron energy spectrum and gas-density profile for different wedge angles. (a) Electron spectra obtained with the 2-mm-wide nozzle. (b) Gas density on the laser axis obtained by our performing hydrodynamic simulation with ANSYS FLUENT.

Comparison with different wedge angles. We explore empirically the effect of different wedge angles using a 2-mm-wide nozzle (see Fig. 4), where the nominal peak energy of the accelerated electron beam is around 160 MeV. The charge of the focused electron beam decreases and the energy spread increases slightly when the 0° and 15° wedges are used but remains roughly the same when the 30° wedge is used (see Table I). As a result, the highest peak charge density is achieved with the 30° wedge. This result demonstrates that the plasma-lens technique works well even with different nozzle sizes. Note that when the wedge is implemented, there are always some low-energy electrons with maximum energy of around 50 MeV with a wedge angle ϕ of 0° or 15° and 15 MeV for ϕ of 30° [see Fig. 4(a)]. A reasonable explanation for the source of the low-energy electrons is that these are injected during the down-ramp of the LPA and are postaccelerated in the wake generated in the low-density bump region [52]. Nevertheless, for our purpose of generating a seeded FEL, those low-energy electrons do not affect the performance of the high-energy beam of interest.

Conclusion. We have demonstrated an integrated plasma lens behind an LPA generated by our modifying the gas flow of a nozzle with a small metal wedge. When optimized, the collimated electron beam has a divergence of less than 1 mrad, while the peak energy and the total charge are preserved. As a result, the peak spectral-charge density increases by more than twofold. The increased beam divergence allowed us to transport the beams and successfully demonstrate LPA-driven FELs

[4]. The focusing effect is attributed mostly to the ion cavity created by the electron beam itself in the density bump, while the linear wakefield generated by the residual drive laser plays a minor role in focusing the beams. This technique unlocks the possibility of achieving adiabatic focusing and staging in a compact setup.

Acknowledgments. Y.-Y.C. thanks E. Levine for initiating the hydrodynamics simulations and Dr. T. Höhne for assisting with the ANSYS FLUENT simulation modeling. The laser-electron acceleration project at Helmholtz-Zentrum Dresden-Rossendorf is fully supported by the Helmholtz Association under the program "Matter and Technology," topic "Accelerator Research and Development." A.G. is financed by Germany's Federal Ministry of Education and Research (BMBF) through the Verbundforschung LADIAG. The authors gratefully acknowledge the Gauss Centre for Supercomputing e.V. (GCS) for funding this project by providing computing time on the GCS supercomputer JUWELS [53] at Jülich Supercomputing Centre. This research used resources of the Oak Ridge Leadership Computing Facility at the Oak Ridge National Laboratory, which is supported by the Office of Science of the U.S. Department of Energy under Contract No. DE-AC05-00OR22725.

[1] E. Esarey, C. B. Schroeder, and W. P. Leemans, Physics of laser-driven plasma-based electron accelerators, Rev. Mod. Phys. **81**, 1229 (2009).

[2] A. Gonsalves, K. Nakamura, J. Daniels, C. Benedetti, C. Pieronek, T. De Raadt, S. Steinke, J. Bin, S. Bulanov, and J. Van Tilborg, Petawatt laser guiding and electron beam acceleration to 8 GeV in a laser-heated capillary discharge waveguide, Phys. Rev. Lett. **122**, 084801 (2019).

[3] W. Wang, K. Feng, L. Ke, C. Yu, Y. Xu, R. Qi, Y. Chen, Z. Qin, Z. Zhang, and M. Fang, Free-electron lasing at 27 nanometres based on a laser wakefield accelerator, Nature **595**, 516 (2021).

[4] M. Labat, J. C. Cabadağ, A. Ghaith, A. Irman, A. Berlioux, P. Berteaud, F. Blache, S. Bock, F. Bouvet, F. Briquez, *et al.*, Seeded free-electron laser driven by a compact laser plasma accelerator, Nat. Photonics **17**, 150 (2023).

[5] C. B. Schroeder, E. Esarey, C. Geddes, C. Benedetti, and W. P. Leemans, Physics considerations for laser-plasma linear colliders, Phys. Rev. ST Accel. Beams **13**, 101301 (2010).

[6] O. Lundh, J. Lim, C. Rechatin, L. Ammoura, A. Ben-Ismaïl, X. Davoine, G. Gallot, J.-P. Goddet, E. Lefebvre, V. Malka, and J. Faure, Few femtosecond, few kiloampere electron bunch produced by a laser–plasma accelerator, Nat. Phys. **7**, 219 (2011).

[7] A. Buck, M. Nicolai, K. Schmid, C. M. S. Sears, A. Sävert, J. M. Mikhailova, F. Krausz, M. C. Kaluza, and L. Veisz, Real-time observation of laser-driven electron acceleration, Nat. Phys. **7**, 543 (2011).

[8] O. Zarini, J. C. Cabadağ, Y.-Y. Chang, A. Köhler, T. Kurz, S. Schöbel, W. Seidel, M. Bussmann, U. Schramm, A. Irman, *et al.*, Multioctave high-dynamic range optical spectrometer for single-pulse, longitudinal characterization of ultrashort electron bunches, Phys. Rev. Accelerators Beams **25**, 012801 (2022).

[9] Y. F. Li, D. Z. Li, K. Huang, M. Z. Tao, M. H. Li, J. R. Zhao, Y. Ma, X. Guo, J. G. Wang, M. Chen, N. Hafz, J. Zhang, and L. M. Chen, Generation of 20 kA electron beam from a laser wakefield accelerator, Phys. Plasmas **24**, 023108 (2017).

[10] J. Couperus, R. Pausch, A. Köhler, O. Zarini, J. Krämer, M. Garten, A. Huebl, R. Gebhardt, U. Helbig, S. Bock, *et al.*, Demonstration of a beam loaded nanocoulomb-class laser wakefield accelerator, Nat. Commun. **8**, 487 (2017).

[11] C. M. Sears, A. Buck, K. Schmid, J. Mikhailova, F. Krausz, and L. Veisz, Emittance and divergence of laser wakefield accelerated electrons, Phys. Rev. ST Accel. Beams **13**, 092803 (2010).

[12] R. Weingartner, S. Raith, A. Popp, S. Chou, J. Wenz, K. Khrennikov, M. Heigoldt, A. R. Maier, N. Kajumba, M. Fuchs, *et al.*, Ultralow emittance electron beams from a laser-wakefield accelerator, Phys. Rev. ST Accel. Beams **15**, 111302 (2012).

[13] P. Antici, A. Bacci, C. Benedetti, E. Chiadroni, M. Ferrario, A. Rossi, L. Lancia, M. Migliorati, A. Mostacci, L. Palumbo, *et al.*, Laser-driven electron beamlines generated by coupling laser-plasma sources with conventional transport systems, J. Appl. Phys. **112**, 044902 (2012).

[14] M. Migliorati, A. Bacci, C. Benedetti, E. Chiadroni, M. Ferrario, A. Mostacci, L. Palumbo, A. Rossi, L. Serafini, and P. Antici, Intrinsic normalized emittance growth in laser-driven electron accelerators, Phys. Rev. ST Accel. Beams **16**, 011302 (2013).

[15] K. Floettmann, Some basic features of the beam emittance, Phys. Rev. ST Accel. Beams **6**, 034202 (2003).

[16] H.-P. Schlenvoigt, K. Haupt, A. Debus, F. Budde, O. Jäckel, S. Pfotenhauer, H. Schwoerer, E. Rohwer, J. Gallacher, E. Brunetti, *et al.*, A compact synchrotron radiation source driven by a laser-plasma wakefield accelerator, Nat. Phys. **4**, 130 (2008).

[17] M. Fuchs, R. Weingartner, A. Popp, Z. Major, S. Becker, J. Osterhoff, I. Cortrie, B. Zeitler, R. Hörlein, G. D. Tsakiris, *et al.*, Laser-driven soft-X-ray undulator source, Nat. Phys. **5**, 826 (2009).

[18] T. André, I. Andriyash, A. Loulergue, M. Labat, E. Roussel, A. Ghaith, M. Khojoyan, C. Thaury, M. Valléau, F. Briquez, *et al.*, Control of laser plasma accelerated electrons for light sources, Nat. Commun. **9**, 1334 (2018).

[19] A. Ghaith, M.-E. Couprie, D. Oumbarek-Espinos, I. Andriyash, F. Massimo, J. Clarke, M. Courthold, V. Bayliss, A. Bernhard, M. Trunk, *et al.*, Undulator design for a laser-plasma-based free-electron-laser, Phys. Rep. **937**, 1 (2021).

[20] P. Chen, A possible final focusing mechanism for linear colliders, Part. Acceler. **20**, 171 (1987).

[21] J. Su, T. Katsouleas, J. Dawson, and R. Fedele, Plasma lenses for focusing particle beams, Phys. Rev. A **41**, 3321 (1990).

[22] H. Nakanishi, Y. Yoshida, T. Ueda, T. Kozawa, H. Shibata, K. Nakajima, T. Kurihara, N. Yugami, Y. Nishida, T. Kobayashi, *et al.*, Direct observation of plasma-lens effect, Phys. Rev. Lett. **66**, 1870 (1991).

[23] G. Hairapetian, P. Davis, C. Clayton, C. Joshi, S. Hartman, C. Pellegrini, and T. Katsouleas, Experimental demonstration of dynamic focusing of a relativistic electron bunch by an overdense plasma lens, Phys. Rev. Lett. **72**, 2403 (1994).

[24] G. Hairapetian, P. Davis, C. Clayton, C. Joshi, C. Pellegrini, and T. Katsouleas, Transverse dynamics of a short, relativistic electron bunch in a plasma lens, Phys. Plasmas **2**, 2555 (1995).

[25] J. Ng, P. Chen, H. Baldis, P. Bolton, D. Cline, W. Craddock, C. Crawford, F. Decker, C. Field, Y. Fukui, *et al.*, Observation of plasma focusing of a 28.5 GeV positron beam, Phys. Rev. Lett. **87**, 244801 (2001).

[26] M. Thompson, H. Badakov, J. Rosenzweig, G. Travish, N. Barov, P. Piot, R. Fliller, G. Kazakevich, J. Santucci, J. Li, *et al.*, Observations of low-aberration plasma lens focusing of relativistic electron beams at the underdense threshold, Phys. Plasmas **17**, 073105 (2010).

[27] C. Thaury, E. Guillaume, A. Döpp, R. Lehe, A. Lifschitz, K. Ta Phuoc, J. Gautier, J.-P. Goddet, A. Tafzi, A. Flacco, *et al.*, Demonstration of relativistic electron beam focusing by a laser-plasma lens, Nat. Commun. **6**, 6860 (2015).

[28] J. Van Tilborg, S. Steinke, C. Geddes, N. Matlis, B. Shaw, A. Gonsalves, J. Huijts, K. Nakamura, J. Daniels, C. Schroeder, *et al.*, Active plasma lensing for relativistic laser-plasma-accelerated electron beams, Phys. Rev. Lett. **115**, 184802 (2015).

[29] S. Kuschel, D. Hollatz, T. Heinemann, O. Karger, M. Schwab, D. Ullmann, A. Knetsch, A. Seidel, C. Rödel, M. Yeung, *et al.*, Demonstration of passive plasma lensing of a laser wakefield accelerated electron bunch, Phys. Rev. Accel. Beams. **19**, 071301 (2016).

[30] C. E. Doss, E. Adli, R. Ariniello, J. Cary, S. Corde, B. Hidding, M. J. Hogan, K. Hunt-Stone, C. Joshi, K. A. Marsh, *et al.*, Laser-ionized, beam-driven, underdense, passive thin plasma lens, Phys. Rev. Accel. Beams. **22**, 111001 (2019).

[31] R. Lehe, C. Thaury, E. Guillaume, A. Lifschitz, and V. Malka, Laser-plasma lens for laser-wakefield accelerators, Phys. Rev. ST Accel. Beams **17**, 121301 (2014).

[32] R. Pompili, M. Anania, M. Bellaveglia, A. Biagioni, S. Bini, F. Bisesto, E. Brentegani, F. Cardelli, G. Castorina, E. Chiadroni, *et al.*, Focusing of high-brightness electron beams with active-plasma lenses, Phys. Rev. Lett. **121**, 174801 (2018).

[33] C. A. Lindstrøm, E. Adli, G. Boyle, R. Corsini, A. Dyson, W. Farabolini, S. Hooker, M. Meisel, J. Osterhoff, J.-H. Röckemann, *et al.*, Emittance preservation in an aberration-free active plasma lens, Phys. Rev. Lett. **121**, 194801 (2018).

[34] A. Gonsalves, K. Nakamura, C. Lin, D. Panasenko, S. Shiraishi, T. Sokollik, C. Benedetti, C. Schroeder, C. Geddes, J. Van Tilborg, *et al.*, Tunable laser plasma accelerator based on longitudinal density tailoring, Nat. Phys. **7**, 862 (2011).

[35] C. Aniculaesei, V. B. Pathak, H. T. Kim, K. H. Oh, B. J. Yoo, E. Brunetti, Y. H. Jang, C. I. Hojbota, J. H. Shin, J. H. Jeon, *et al.*, Electron energy increase in a laser wakefield accelerator using up-ramp plasma density profiles, Sci. Rep. **9**, 11249 (2019).

[36] M. Hansson, B. Aurand, X. Davoine, H. Ekerfelt, K. Svensson, A. Persson, C.-G. Wahlström, and O. Lundh, Down-ramp injection and independently controlled acceleration of electrons in a tailored laser wakefield accelerator, Phys. Rev. ST Accel. Beams **18**, 071303 (2015).

[37] L. Ke, K. Feng, W. Wang, Z. Qin, C. Yu, Y. Wu, Y. Chen, R. Qi, Z. Zhang, Y. Xu, *et al.*, Near-GeV electron beams at a few per-mille level from a laser wakefield accelerator via density-tailored plasma, Phys. Rev. Lett. **126**, 214801 (2021).

[38] ANSYS, *ANSYS Fluent Theory Guide* (ANSYS Inc., PA, 2013).

[39] J. Couperus, A. Köhler, T. Wolterink, A. Jochmann, O. Zarini, H. Bastiaens, K. Boller, A. Irman, and U. Schramm, Tomographic characterisation of gas-jet targets for laser wakefield acceleration, Nucl. Instrum. Methods Phys. Res., Sect. A **830**, 504 (2016).

[40] A. Koehler, R. Pausch, M. Bussmann, J. C. Cabadağ, A. Debus, J. Krämer, S. Schöbel, O. Zarini, U. Schramm, and A. Irman, Restoring betatron phase coherence in a beam-loaded laser-wakefield accelerator, Phys. Rev. Accel. Beams. **24**, 091302 (2021).

[41] U. Schramm, *et al.*, First results with the novel petawatt laser acceleration facility in Dresden, J. Phys.: Conf. Ser. **874**, 012028 (2017).

[42] T. Kurz, J. P. Couperus, J. M. Krämer, H. Ding, S. Kuschel, A. Köhler, O. Zarini, D. Hollatz, D. Schinkel, R. D'Arcy, *et al.*, Calibration and cross-laboratory implementation of scintillating screens for electron bunch charge determination, Rev. Sci. Instrum. **89**, 093303 (2018).

[43] M. Zeng, M. Chen, Z.-M. Sheng, W. B. Mori, and J. Zhang, Self-truncated ionization injection and consequent monoenergetic electron bunches in laser wakefield acceleration, Phys. Plasmas **21**, 030701 (2014).

[44] M. Tzoufras, W. Lu, F. S. Tsung, C. Huang, W. B. Mori, T. Katsouleas, J. Vieira, R. A. Fonseca, and L. O. Silva, Beam loading in the nonlinear regime of plasma-based acceleration, Phys. Rev. Lett. **101**, 145002 (2008).

[45] P. C. Rocha, H. B. Rocha, F. M. Carneiro, M. V. Da Silva, and A. V. Bueno, k-ω SST (shear stress transport) turbulence model calibration: A case study on a small scale horizontal axis wind turbine, Energy **65**, 412 (2014).

[46] See Supplemental Material at http://link.aps.org/supplemental/10.1103/PhysRevApplied.20.L061001 for the ANSYS FLUENT simulation settings and the theoretical optimum performance of the integrated plasma lens.

[47] M. Bussmann, H. Burau, T. E. Cowan, A. Debus, A. Huebl, G. Juckeland, T. Kluge, W. E. Nagel, R. Pausch, F. Schmitt, *et al.*, in *Proceedings of the International Conference on High Performance Computing, Networking, Storage and Analysis* (2013), p. 1.

[48] Pic-analysis, https://doi.org/10.14278/rodare.2359 (accessed 2023-July-03).

[49] Pic-settings, https://doi.org/10.14278/rodare.2361 (accessed 2023-July-03).

[50] R. Lehe, C. Thaury, A. Lifschitz, J.-M. Rax, and V. Malka, Transverse dynamics of an intense electron bunch traveling through a pre-ionized plasma, Phys. Plasmas **21**, 043104 (2014).

[51] H. Wiedemann, *Particle Accelerator Physics* (Springer, Cham, 2015).

[52] T. Kurz, T. Heinemann, M. Gilljohann, Y. Chang, J. Couperus Cabadağ, A. Debus, O. Kononenko, R. Pausch, S. Schöbel, R. Assmann, *et al.*, Demonstration of a compact plasma accelerator powered by laser-accelerated electron beams, Nat. Commun. **12**, 2895 (2021).

[53] Jülich Supercomputing Centre, JUWELS cluster and booster: Exascale pathfinder with modular supercomputing architecture at Juelich Supercomputing Centre, J. Large-Scale Res. Facil. **7**, A183 (2021).